

THE EFFECT OF MICROLENSING ON THE OBSERVED X-RAY ENERGY SPECTRA OF GRAVITATIONALLY LENSED QUASARS

H. KRAWCZYNSKI,¹ G. CHARTAS,^{2,3} AND F. KISLAT⁴

¹*Physics Department and McDonnell Center for the Space Sciences, Washington University in St. Louis, 1 Brookings Drive, CB 1105, St. Louis, MO 63130*

²*Department of Physics and Astronomy, College of Charleston, Charleston, SC, 29424, USA*

³*Department of Physics and Astronomy, University of South Carolina, Columbia, SC, 29208*

⁴*Department of Physics & Space Science Center University of New Hampshire, Durham, NH 03824*

Submitted to ApJ

ABSTRACT

The *Chandra* observations of several gravitationally lensed quasars show evidence for flux and spectral variability of the X-ray emission that is uncorrelated between images and is thought to result from the microlensing by stars in the lensing galaxy. We report here on the most detailed modeling of such systems to date, including simulations of the emission of the Fe K α fluorescent radiation from the accretion disk with a general relativistic ray tracing code, the use of realistic microlensing magnification maps derived from inverse ray shooting calculations, and the simulation of the line detection biases. We use lensing and black hole parameters appropriate for the quadruply lensed quasar RX J1131–1231 ($z_s = 0.658$, $z_l = 0.295$), and compare the simulated results with the observational results. The simulations cannot fully reproduce the distribution of the detected line energies indicating that some of the assumptions underlying the simulations are not correct, or that the simulations are missing some important physics. We conclude by discussing several possible explanations.

Keywords: accretion, accretion disks, black hole physics, black hole physics, gravitational lensing: micro, line: formation, line: profiles, (galaxies:) quasars: emission lines, (galaxies:) quasars: general, (galaxies:) quasars: individual (QSO RX J1131–1231), (galaxies:) quasars: supermassive black holes

1. INTRODUCTION

The gravitational lensing of the emission from distant quasars produces several macroimages of the quasar with possible substructure on micro-arcsecond and milli-arcsecond scales owing to the discrete nature of the stellar component and the clumpy nature of the dark matter components of the lensing galaxy, respectively (see the review by Wambsganss 2006). The micro, mili, and macro images correspond to the stationary paths of the Fermat potential (or time delay function) generated by the stars, clumpy dark matter and stars, and the entire galaxy, respectively (e.g. Paczyński 1986; Blandford & Narayan 1986; Wambsganss & Paczyński 1992; Yonehara et al. 2003). The motion of the deflectors relative to the line of sight results in uncorrelated brightness fluctuations of the macroimages as the caustic folds and cusps created by the granular mass distribution move across the source, each flare corresponding to the appearance or disappearance of two microimages.

Observations of the microlensing brightness fluctuations of quasars have been used to constrain the sizes of the quasar emission regions as the amplitude of the microlensing flux variability depends on the ratio of the angular radius of the source to the Einstein radius α_0 (two angles). The latter is given by: (e.g. Schneider et al. 1992):

$$\alpha_0 = \sqrt{\frac{4G \langle M_* \rangle}{c^2} \frac{D_{LS}}{D_L D_S}}. \quad (1)$$

where $\langle M_* \rangle$ is the average mass of the deflecting stars, and D_{LS} , D_L , and D_S are the angular diameter distances between the lens and the source, the observer and the lens, and the observer and the source, respectively. Whereas the observations indicate that the optical/UV bright portions of the accretion disks might be significantly larger than predicted by thin disk theory (Morgan et al. 2010), the X-ray bright accretion disk coronae seem to be extremely compact, i.e. smaller than $30 r_g$ with $r_g = GM/c^2$ being the gravitational radius of the black hole (Chartas et al. 2009; Dai et al. 2010; Morgan et al. 2012; Mosquera et al. 2013; Blackburne et al. 2015; MacLeod et al. 2015). These X-ray microlensing constraints are independent and complimentary to spectral (e.g. Wilms et al. 2001; Fabian et al. 2009; Zoghbi et al. 2010; Parker et al. 2014; Chiang et al. 2015) and reverberation (e.g. Zoghbi et al. 2014; Cackett et al. 2014; Uttley et al. 2014) constraints on the corona sizes of nearby (unlensed) Narrow Line Seyfert I (NRLS I) active galactic nuclei (AGNs).

Even well before the observational discovery of microlensing flux variability, various authors remarked on the possibility of using quasar microlensing to constrain

the stellar component (e.g. Webster et al. 1991; Lewis & Irwin 1996). Several years later, Schechter & Wambsganss (2002) used the inverse ray shooting (RS) method (Young 1981; Paczyński 1986; Schneider & Weiss 1987; Kayser et al. 1986; Wambsganss 1999) to generate a series of microlensing magnification maps for different ratios of stellar to dark matter masses. The authors found that the smooth mass component enhanced the amplitude of the brightness fluctuations. Comparing the flux variations of the images corresponding to the saddle points of the Fermat potential to those of the images corresponding to the minima of the Fermat potential showed that saddle point images exhibited larger brightness fluctuations than minimum images in agreement with the earlier result of Witt (1995); Metcalf & Madau (2001).

More recently, Pooley et al. (2012) analyzed 61 observations of 14 quadruply lensed quasars observed with the *Chandra* X-ray satellite with the aim to constrain the stellar to dark matter mass ratio. They argued that X-ray observations were better suited than optical observations (e.g. Kochanek & Dalal 2004; Schechter et al. 2004b) as the angular extents of the X-ray emission regions were smaller than the Einstein radius of the stars. The authors used for each image the convergence κ and shear γ from the analysis of the positions of the macroimages, and ran a series of RS simulations for different stellar convergence to total convergence fractions. Using the magnification probability distributions from the RS simulations and the a priori probability distribution of the intrinsic quasar brightness fluctuations from deep studies of the cosmic X-ray background, they inferred a mean stellar (dark matter) contribution to the total convergence of 7% (93%) (see Schechter et al. 2014; Jiménez-Vicente et al. 2015, for related studies).

In this paper, we focus on using the RS method to simulate the spectral shapes of the microlensed Fe K α emission from quasars. The Fe K α emission is thought to originate from a hot X-ray bright corona illuminating the accretion disk with high energy X-rays, prompting the emission of fluorescent Fe K α photons (see Reynolds 2014, and references therein). As the energies of the escaping Fe K α photons depend on the Doppler and gravitational frequency shifts between emission and detection, the photon energies encode information about where the photons originated in the accretion disk and about the background spacetime. A caustic fold crossing the accretion disk selectively amplifies the emission from a narrow slice of the accretion disk and produces energy spectra carrying the imprint of the Doppler and gravitational frequency shifts characteristic for the emission from this slice. Chartas et al. (2002) present sim-

ulated microlensed Fe $K\alpha$ energy spectra accounting for Doppler and gravitational frequency shifts using the general parameterization of the magnification close to caustic folds (e.g. Schneider et al. 1992):

$$\mu/\mu_0 = 1 + \frac{K}{\sqrt{y_\perp}} H(y_\perp) \quad (2)$$

with y_\perp being (up to the sign) the distance from the fold located at $y_\perp = 0$, K encoding the lens properties, and the Heaviside step function $H(y_\perp) = 0$ for $y_\perp < 0$ and $H(y_\perp) = 1$ for $y_\perp \geq 0$. The simulations predict distorted energy spectra with one or two spectral peaks.

The *Chandra* observations of the quadruply lensed quasars RX J1131–1231 ($z_s = 0.658$, $z_l = 0.295$) and SDSS 1004+4112 ($z_s = 1.734$, $z_l = 0.68$), the double lens quasar QJ 0158–4325 ($z_s = 1.294$, $z_l = 0.317$) (Chartas et al. 2012, 2017), and to lesser degree the quasar MG J0414+0534 ($z_s = 2.64$, $z_l = 0.96$) (Chartas et al. 2002) seem to confirm these predictions, showing energy spectra deviating from an absorbed power law model which can be fit with a model assuming one or two emission lines with line centroids changing from observation to observation. Based on estimates of the masses of the three black holes and the effective velocity of the caustic patterns across the quasars, Chartas et al. (2017) estimate that caustic folds cross the central $10r_g$ regions of the accretion flows of the three quasars within 0.6 to 2.9 months, implying that some of the *Chandra* observations recorded energy spectra from different stages of the crossing of a single caustic fold moving across the inner portion of the accretion disk. The authors remark that the range of the observed line centroids and the ratio of the two line centroids for energy spectra with two spectral lines can be used to constrain the inclination and spin of the black hole.

Various authors discuss more detailed simulations of the Fe $K\alpha$ emission. Popović et al. (2003, 2006) use a general relativistic (GR) ray tracing code to predict the line shapes. The authors assume that the Fe $K\alpha$ emissivity of the equatorial accretion disk either follows a power law dependence in the radial Boyer Lindquist coordinate r or is proportional to the thermal emissivity. Jovanović et al. (2009) perform similar simulations focussing on the impact of an absorber covering parts of the accretion disk. The authors use generic parameterizations of the magnification close to a caustic fold, and a few realizations of RS magnification maps. Neronov & Vovk (2016) perform similar simulations and study the time evolution of the energy spectra during individual caustic crossings and posit that dense spectroscopic observations of such caustic crossings may present a new method for testing general relativity based on X-ray ob-

servations (however, see Krawczynski 2018, for a critical discussion of the magnitude and impact of astrophysical uncertainties). In an earlier paper (Krawczynski & Chartas 2017, called Paper I in the following) we use a GR raytracing code to simulate the illumination of a geometrically thin accretion disk by a lamppost corona located at a height h above the accretion disk. Combining these simulations with the magnification from Equation (2), we discuss the distribution of the centroids and widths of the observed emission lines, and in the case of energy spectra with two emission lines, the ratio of the two peak energies as function of the black hole spin, the inclination of the accretion disk relative to the observer, the lamppost height h , the magnification parameter K , and the location and orientation of the caustic folds.

The present paper examines the statistical properties of the distorted Fe $K\alpha$ lines, i.e. the likelihood of detecting shifted or double spectral peaks. We do so by combining the results of the GR raytracing simulations of the Fe $K\alpha$ emission with magnification maps from RS calculations. The study presented here is closely related to the earlier studies of Lewis & Irwin (1996); Schechter & Wambsganss (2002); Schechter et al. (2004a); Pooley et al. (2012); Schechter et al. (2014); Jiménez-Vicente et al. (2015) mentioned above as the observed properties depend on the source parameters *and* the microlensing parameters. Eventually, we would like to examine the outer product of the parameter spaces describing the black hole, the accretion disk, the X-ray bright corona, and the microlensing, and evaluate which parameter combination describes the X-ray data best. The comparison of the simulated and observed data would then constrain the properties of the quasar and the lensing galaxy, including the properties of the stellar and dark matter components.

We limit the scope of this paper to considering only a small portion of the quasar and lensing parameter spaces, and studying qualitatively if the simulated Fe $K\alpha$ energy spectra can explain the observed phenomenology. The observational results will be summarized in §2 and the numerical simulation methods will be presented in §3. Simulated magnification maps are presented in §4 and simulated Fe $K\alpha$ energy spectra are discussed in §5. Finally, we use the simulated Fe $K\alpha$ energy spectra to generate simulated *Chandra* data sets. We fit the simulated and observed *Chandra* spectra of RX J1131–1231 in the same manner using an automated script described in §6. The paper concludes with a summary and discussion of the results in §7.

In the following, we assume the cosmological parameters from the 2015 Planck release Planck Collaboration (2016), i.e. a Hubble constant $H_0 = 67.8 \text{ km s}^{-1} \text{ Mpc}^{-1}$,

Source	<i>Chandra</i> Pointings	Image	Spectra with detected lines (>99% CL)	Spectra with 2 detected lines (both >99% CL)
RX J1131–1231	38	A (HS)	7	1
		B (HM)	5	0
		C (LM)	4	2
		D (LS)	2	0
SDSS 1004+4112	10	A (HS)	1	1
		B (HM)	1	0
		C (LM)	1	0
		D (LS)	2	0
Q J0158–4325	12	A (HM)	2	1
		B (LM)	0	0

Table 1. Statistics of the *Chandra* Fe K α detections. See (Chartas et al. 2017) for details.

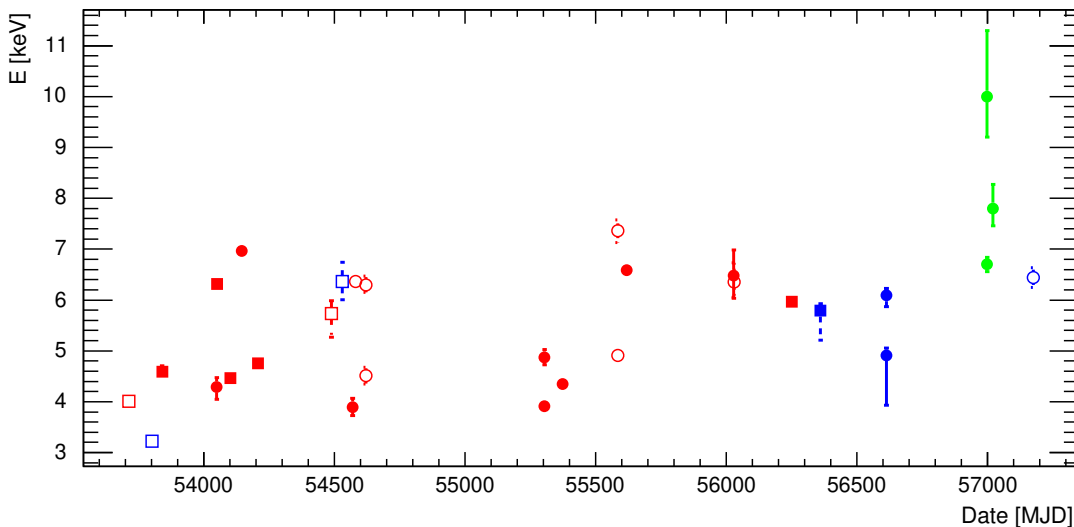


Figure 1. Distribution of the detected rest frame line centroid energies as a function in time for RX J1131–1231 (red), SDSS 1004+4112 (blue) and QJ 0158–4325 (green) for image A (full circles), image B (full squares), and if present, image C (open circles) and image D (open squares) of the respective sources. We show only lines detected on a >99% confidence level and 90% confidence interval error bars. The times of the images have been corrected for the measured or estimated time offsets of the individual images. RX J1131–1231: Images B and C lead image A by 0.7 and 1.1 days, respectively, and image D lags image A by 91 days (Tewes et al. 2013); SDSS 1004+4112: Images B and C lead image A by 41 and 822 days, respectively, and image D lags image A by 1789 days (Fohlmeister et al. 2008, 2013); QJ 0158–4325: Image B lags image A by 14.5 days (Faure et al. 2009).

a matter density of $\Omega_m/\Omega_c = 30.9\%$, and a dark energy density $\Omega_\Lambda/\Omega_c = 69.1\%$, with Ω_c being the critical density.

If not mentioned otherwise, we use geometric units ($G=c=1$). Distances in physical units are given in units of the gravitational radius $r_g = GM_{\text{BH}}/c^2$ with M_{BH} being the black hole mass. Denoting the angu-

lar momentum by J , the spin parameter is given by $a = J/cr_g M_{\text{BH}} = cJ/GM_{\text{BH}}^2$. In units of M_{BH} , the spin parameter a can range from -1 to +1.

2. OBSERVATIONAL RESULTS

The three quasars with the best evidence for time variable Fe K α lines are the quadruply lensed quasars

RX J1131–1231 and SDSS 1004+4112 and the double lens quasar QJ 0158–4325 (see Chartas et al. 2017, for details). Table 1 summarizes the number of *Chandra* observations, and for each macro image the number of observations with highly significant (>99% confidence level) single and double Fe K α line detections. We identify the images here with their letters A-D. For each image we note if it corresponds to the higher magnification saddle point (HS), the lower magnification saddle point (LS), the higher magnification minimum (HM), or the lower magnification minimum (LM) of the Fermat potential. The highly significant lines were detected in 12%, 13%, and 8% of the energy spectra of RX J1131–1231, SDSS 1004+4112, and QJ 0158–4325, respectively. Highly significant double peaks were detected in 2%, 2.5%, and 4% of the energy spectra of the three sources, respectively.

Figure 1 shows for all three sources the rest frame centroids of the detected lines as a function of time. Thirteen (43%) of the detected lines have centroid energies below 5 keV, fifteen (50%) have energies between 5.6 keV and 7.4 keV, and two (7%) have energies exceeding 7.6 keV. Figure 2 shows the distribution of the line centroids for image A of RX J1131–1231, exhibiting two peaks, one at ~ 4 keV, and one at ~ 7 keV. Considering only the sample of < 5 keV line detections, Figure 1 reveals some weak evidence for a clustering of the detections in time, i.e. for image B of RX J1131–1231 three < 5 keV lines were detected before MJD 54,250, and none afterwards, and for image A of the same source only one < 5 keV line was detected before MJD 54,250, and four afterwards.

3. NUMERICAL METHODS

3.1. General Relativistic Ray Tracing Code

Our GR ray tracing code has been described in (Krawczynski 2012; Hoormann et al. 2016; Beheshtipour et al. 2016, 2017; Krawczynski & Chartas 2017). It uses the Kerr metric in Boyer Lindquist (BL) coordinates $x^\mu = (ct, r, \theta, \phi)$ with ct and r in units of r_g . A lamp-post corona (Matt et al. 1991) close to the spin axis of the black hole hovers at $r = 5 r_g$ above the black hole and emits photon packets isotropically in its rest frame. The photon packets are tracked until they impinge on a geometrically thin accretion disk extending from the Innermost Stable Circular Orbit (ISCO) to $100 r_g$. The 0-component of the photon packet’s wave vector k^μ is initially set to 1 and is used to keep track of the frequency shift along the packet’s trajectory. Each photon packet represents a power law distribution of initially unpolarized corona photons with differential spectral index $\Gamma = 1.7$ (from $dN/dE \propto E^{-\Gamma}$). The position

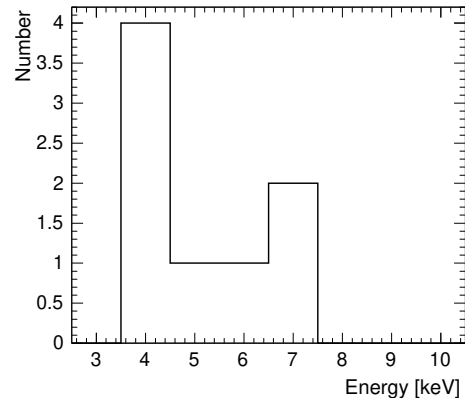


Figure 2. Distribution of the rest frame centroid energies for all lines of image A of RX J1131–1231 detected at a $> 99\%$ confidence level.

and wave vectors are evolved forward in time by integrating the geodesic equation with an adaptive stepsize Cash-Karp method. The code keeps track of the photon packets’ polarization by storing the polarization fraction and vector. The polarization fraction is modified every time the photon scatters, and the polarization vector is parallel transported along the photon packets’ geodesic.

Photon packets impinging on the accretion disk at $\theta = \pi/2$ are absorbed, scatter, or prompt the emission of an Fe K α photon. We adopt a phenomenological parameterization for the relative probabilities of these three processes with an absorption probability of $p_{\text{abs}} = 0.9$ per encounter, and equal probabilities for scattering and for the production of a Fe K α photon packets. Scattering off the accretion disk is implemented by first transforming the photon packet’s wave and polarization vectors from the BL coordinates into the reference frame of the accretion disk plasma. Subsequently, the photon packet scatters as described by the formalism of Chandrasekhar (1960) for the reflection of polarized emission off an indefinitely thick electron atmosphere. After scattering, the photon packet’s wave and polarization vectors are back-transformed into the global BL coordinate frame.

The emission of Fe K α photon packets is implemented in a similar way. After transforming the wave and polarization vectors of the photon packet impinging onto the accretion disk into the reference frame of the accretion disk plasma, we use the packet’s 0-component k^0 of the wavevector in the plasma frame to calculate the statistical weight of the emitted Fe K α photon packet according to the assumed power law distribution of the coronal emission (weight $\propto (k^0)^{\Gamma-1}$). The mono-energetic Fe K α

photon packet is emitted with a limb brightening weight and an initial polarization given by Chandrasekhar’s results for the emission of an indefinitely deep electron scattering atmosphere (Chandrasekhar 1960). In the final step, the packet’s wave and polarization vectors are back-transformed into the global BL frame. Photons are tracked until their radial Boyer Lindquist coordinate drops below 1.02 times the r -coordinate of the event horizon (at which point we assume that the photon will disappear into the black hole) or reach a fiducial observer at $r_{\text{obs}} = 10,000 r_g$. In the latter case, the wave and polarization vectors are transformed into the coordinate system of a coordinate stationary observer, and the photon-packets’ position and wavevectors are stored.

For an observer at coordinates r_{obs} , θ_{obs} , and ϕ_{obs} we select all photons recorded in a θ -window from $\theta_{\text{obs}} \pm 2.5^\circ$ and arbitrary ϕ (making use of the problem’s azimuthal symmetry), and backproject each ray onto a plane at $10,000 r$ from the observer assuming a flat spacetime to create a virtual polychromatic image. The virtual images are subsequently convolved with the magnification maps from the RS code (see Krawczynski & Chartas 2017, for a justification of the method).

3.2. Generation of Magnification Maps with an Ray Shooting Code

Our implementation of the RS technique is similar to that described by Schneider & Weiss (1987). Microlensing magnification maps are generated by tracking photons backwards in time from a regular grid in the lens plane to the source plane. The local density of the endpoints of rays in the source plane is proportional to the cross section of the lens for deflecting rays from this location to the observer, and thus to the magnification μ . Given the coordinate \mathbf{x} of a ray in the lens plane the source plane position \mathbf{y} is given by the lens equation:

$$\mathbf{y} = \begin{pmatrix} 1 - \kappa_c - \gamma & 0 \\ 0 & 1 - \kappa_c + \gamma \end{pmatrix} \mathbf{x} - \sum_{i=1}^{N_*} \frac{m_i (\mathbf{x} - \mathbf{x}_i)}{|\mathbf{x} - \mathbf{x}_i|^2}. \quad (3)$$

Here, \mathbf{x} is given in units of the Einstein radius in the lens plane:

$$\xi_0 = \alpha_0 D_L \quad (4)$$

and \mathbf{y} in units of the Einstein radius in the source plane:

$$\zeta_0 = \alpha_0 D_S. \quad (5)$$

The first term on the right side of the lens equation models the light deflection by the galaxy in quadrupole approximation with κ_c being the surface density of the smooth matter distribution and distant stars in units of

the critical density:

$$\Sigma_0 = \left(\frac{4\pi G D_L D_{LS}}{c^2 D_S} \right)^{-1} \quad (6)$$

and γ is the shear parameter. The second term models the deflection from $N_* = \kappa_* A_L / \pi$ nearby stars randomly distributed over a lens plane area A_L with the masses $m_i < M_*$ with $\frac{1}{N} \sum m_i = 1$. The stellar masses m_i are generated according to a power law mass function $dN/dm \propto m^{-1.3}$ for $m \in [m_{\text{min}}, m_{\text{max}}]$ with $m_{\text{max}}/m_{\text{min}} = 50$, matching the Galactic disk mass function (Gould 2000; Poindexter & Kochanek 2010). The angular diameter distance of a source at redshift z_2 seen by an observer at redshift z_1 is given by (Peebles 1993; Hogg et al. 2000):

$$D(z_1, z_2) = \frac{c}{H(z_1)} \frac{1 + z_1}{1 + z_2} \int_{z_1}^{z_2} \frac{dz'}{E(z')} \quad (7)$$

with $E(z)$ and $H(z)$ given by:

$$E(z) = \sqrt{\Omega_m (1+z)^3 + \Omega_\Lambda}. \quad (8)$$

and

$$H(z) = H_0 E(z). \quad (9)$$

For RX J1131–1231 and $\langle M_* \rangle = 0.1 M_\odot$ we obtain: $D_L = 2.9 \times 10^{27}$ cm, $D_S = 4.6 \times 10^{27}$ cm, $D_{LS} = 2.6 \times 10^{27}$ cm, $\xi_0 = 9.8 \times 10^{15}$ cm, and $\zeta_0 = 1.5 \times 10^{16}$ cm. Assuming a black hole mass of $10^8 M_\odot$, $\zeta_0 = 1046 r_g$ ($r_g = 0.000956 \zeta_0$).

The rays are generated over a large lens plane “source area” of (dimensionless) width L_1 and height L_2 to cover an approximately square-shaped “target area” of (dimensionless) width and height $L_s = 8$ in the source plane. The source area is chosen to be sufficiently large so that rays originating outside of the source area have a negligibly small likelihood of ending in the target area. For this purpose, we start with $L_1 \approx f_0 f_1 L_s$ and $L_2 \approx f_0 f_2 L_s$. The factor $f_0 = 5$ assures that the rays cover a sufficiently large area in the source plane (much larger than actually needed), and the factors $f_1 = |1 - (\kappa_c - \gamma)|^{-1}$ and $f_2 = |1 - (\kappa_c + \gamma)|^{-1}$ account for the scaling of distances between the source and lens planes. We distribute stars over a 4 times larger lens plane area to make sure that all rays are surrounded by a large number of stars. Two methods are used to speed up the calculation (see Schneider & Weiss 1987; Wambsganss 1999, for similar approaches). In the first iteration, we shoot 1 million rays and tag all the lens plane locations whose rays end up in the target area. The second iteration is then limited to regions surrounding the tagged portions of the lens plane. The second ray shooting iteration uses a finer mesh, i.e. we

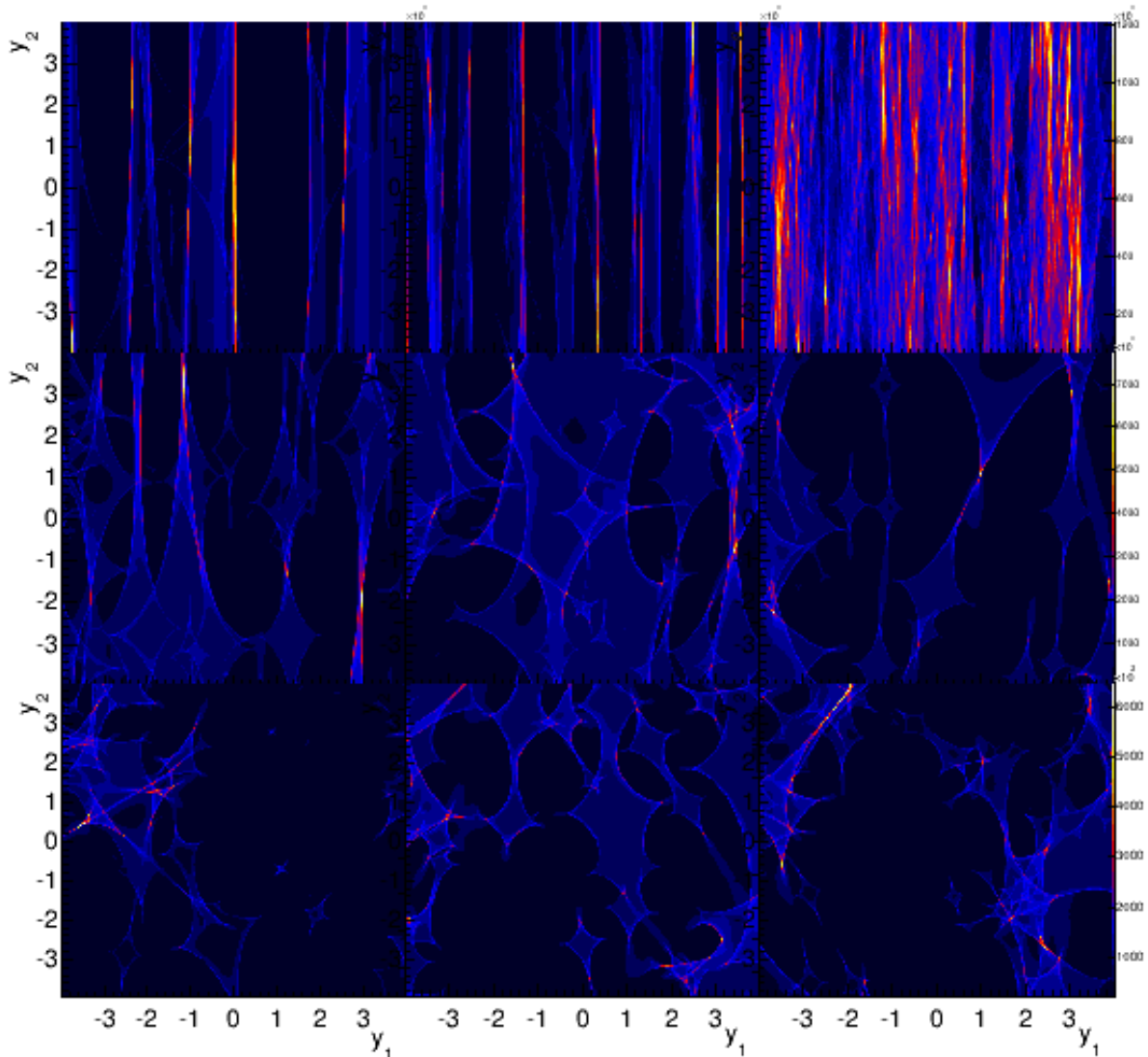


Figure 3. Simulated magnification maps for the bright saddle point (HS) image A of RX J1131–1231 for different splits of the total convergence κ between stellar convergence $\kappa_* = g_*\kappa$ and the smooth convergence $\kappa_c = (1 - g_*)\kappa$ with $g_* = 0.025, 0.05, 0.1, 0.25, 0.5, 0.75, 0.9, 0.95,$ and 0.975 (starting in the upper left corner and going row-wise from the left to the right).

shoot 200×200 rays for each tagged ray of the first iteration. The shooting of the 200×200 rays spread over an area $(\Delta x)^2$ in the lens plane (Δx being the lens plane distance between adjacent rays of the first iteration) is accelerated by dividing the stars into nearby stars (distance $< 30 \Delta x$) and distant (all other) stars. For each ray the deflections from all nearby stars are calculated exactly, and the deflections from all other stars and the macrolens are calculated with a bilinear interpolation using the deflections at the four corners of the considered area. For all our calculations, we check the accuracy of the interpolation scheme for a small fraction of all rays by calculating the deflection by straight summation over all stars. We find the errors to be negligibly

small (< 0.01 in units of the gravitational radius of the black hole). We store “overview” magnification maps on different scales (side lengths of 100, 10, 1, and 0.02 in dimensionless units), sample slices through the maps, and forty $400 r_g$ diameter regions randomly distributed over the central portion of the magnification maps. Random portions of the latter maps are subsequently folded with the virtual quasar images to generate microlensed energy spectra.

4. PROPERTIES OF THE RAY SHOOTING MAGNIFICATION MAPS

We generated magnification maps using for each image the total convergence κ and shear γ from the analysis of (Blackburne et al. 2011; Pooley et al. 2012). The

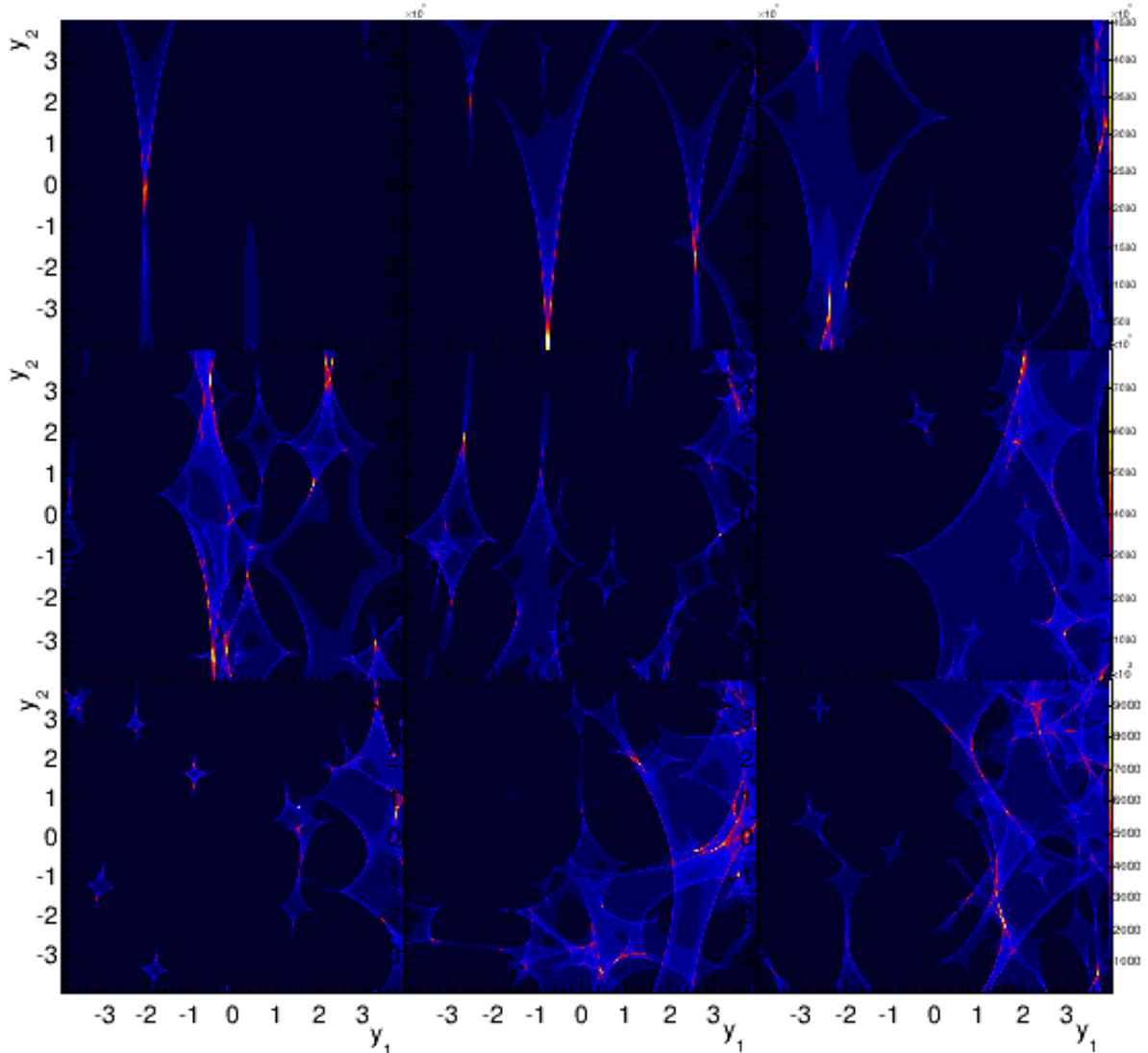


Figure 4. Same as Figure 3 but for the bright minimum (HM) image B of RX J1131–1231.

authors derived the lens parameters with the code of Keeton (2001) based on the positions of the macroimages and neglecting the observed fluxes and time delays. Using the same approach as Pooley et al. (2012), we generated for each image a series of magnification maps using different combinations of the smooth convergence $\kappa_c = (1 - g_*)\kappa$ and the convergence from the stellar component $\kappa_* = g_*\kappa$ with $g_* = 0.025, 0.05, 0.1, 0.25, 0.5, 0.75, 0.9, 0.95,$ and 0.975 .

Figure 3 shows the magnification maps for the bright saddle point (HS) image A ($\kappa = 0.442, \gamma = 0.597$). The density of the caustics in the source plane increases as the fraction of the convergence in stars increases from $g_* = 2.5\%$ to 5% and 10% . For larger g_* -values the caustic density decreases markedly. The behavior contrasts with that of Figure 2 of Schechter & Wambsganss (2002)

where the caustic density increases monotonically with g_* . The difference is that the macro-models considered here have a substantial shear and very large magnification factors $|1/(1 - (\kappa + \gamma))| \approx 26$ along one direction. We find that for constant overall convergence and shear, the model with the largest stellar density per dimensionless source plane area (accounting for the scaling between distances in the lens plane and in the source plane):

$$\kappa_{*,s} = \frac{\kappa_*}{|(1 - \kappa_c - \gamma)(1 - \kappa_c + \gamma)|} \quad (10)$$

produces the highest caustic density in the source plane. We obtain a better correlation of $\kappa_{*,s}$ with the caustic density when scaling between the lens plane and source plane areas with κ_c rather than with the overall convergence $\kappa = \kappa_c + \kappa_*$ in the denominator of Equation (10).

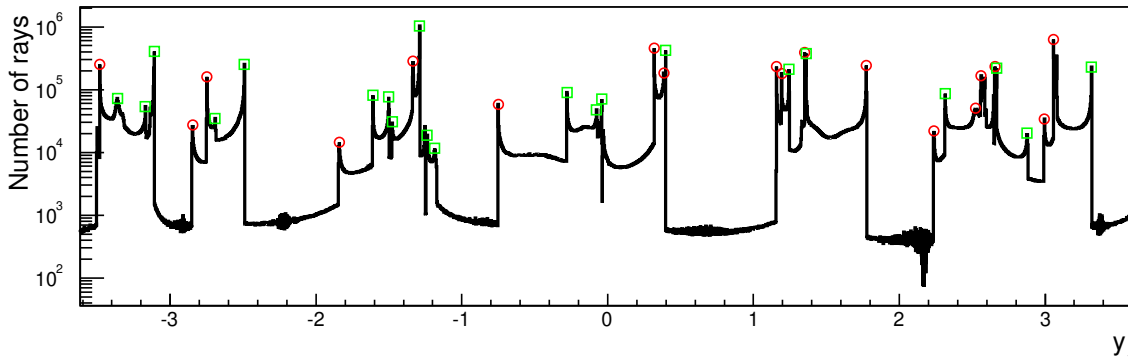


Figure 5. Slice along the y_1 -direction (from left to right) of the magnification map of the bright saddle point (HS) image A, showing the number of traced rays as function of y_1 for $g_* = 5\%$ ($\kappa_c = 0.42$, $\gamma = 0.597$, and $\kappa_* = 0.0221$). The circles and squares show caustics detected by a caustic finding algorithm with circles (squares) being identified as a caustic when searching for magnification steps from left to right (right to left). Some caustics are found twice in which case the algorithm only stores one of the detections.

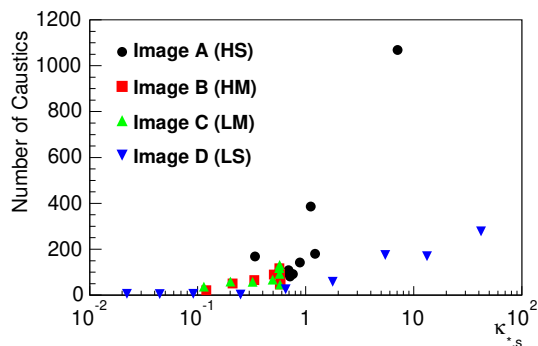


Figure 6. Number of caustics found in slices through the simulated magnification maps of images A-D of RX J1131–1231 as function of the scaled convergence in stars $\kappa_{*,s}$ (see text). The high and low saddle point images (HS, LS) behave qualitatively differently than the minimum images (HM, LM).

The stellar convergence κ_* contributes to focusing light rays, but does not contribute in the same way to the scaling between the density of stars and the density of caustics in the source plane. The source plane statistics of caustics for the cases of $\kappa \pm \gamma \approx 1$ seems to be an interesting topic for future investigations.

Figure 4 shows the magnification maps for image B ($\kappa = 0.423$, $\gamma = 0.507$). In accord with the earlier results of Witt (1995); Metcalf & Madau (2001); Schechter & Wambsganss (2002), we find that the magnification values vary more markedly for the saddle point image A (Figure 3) than for the minimum image B (Figure 4). We developed an algorithm to identify caustics in

$30 r_g$ wide slices through the caustics maps running horizontally from left to right in Figs. 3 and 4. The algorithm exponentially averages the magnification running from left to right (averaging over all bins to the left of a considered point, using for each point a weight which decreases exponentially with the distance from the point) and from right to left, and then identifies caustics through the peaks in the difference distribution. Figure 5 shows the magnifications for an exemplary slice of the magnification map of Fig. 3 together with the caustics that the algorithm identified. Figure 6 summarizes the results from analyzing slices through all the magnification maps, namely the number of detected caustics as a function of $\kappa_{*,s}$. We see that the number of caustics indeed correlate well with $\kappa_{*,s}$. Each image shows a slightly different correlation, with those of the saddle point images A and D exhibiting a qualitatively different behavior than the minimum images B and C. The scatter in the distribution comes from the finite size of the simulated magnification maps.

5. SIMULATION OF THE MICROLENSED FE $K\alpha$ EMISSION

In the previous section we showed the magnification maps for rather large source plane regions, when comparing the width or height ($L_s = 8$ in dimensionless source plane units) of the maps with the size scale of the inner accretion disk of several r_g (with $r_g \approx 0.001$ for RX J1131–1231 in dimensionless source plane units). Simulating such large maps is not a choice but a necessity for assuring that the RS method uses a sufficiently large number of stars to lead to acceptable small number statistics and edge effects. In this section we present

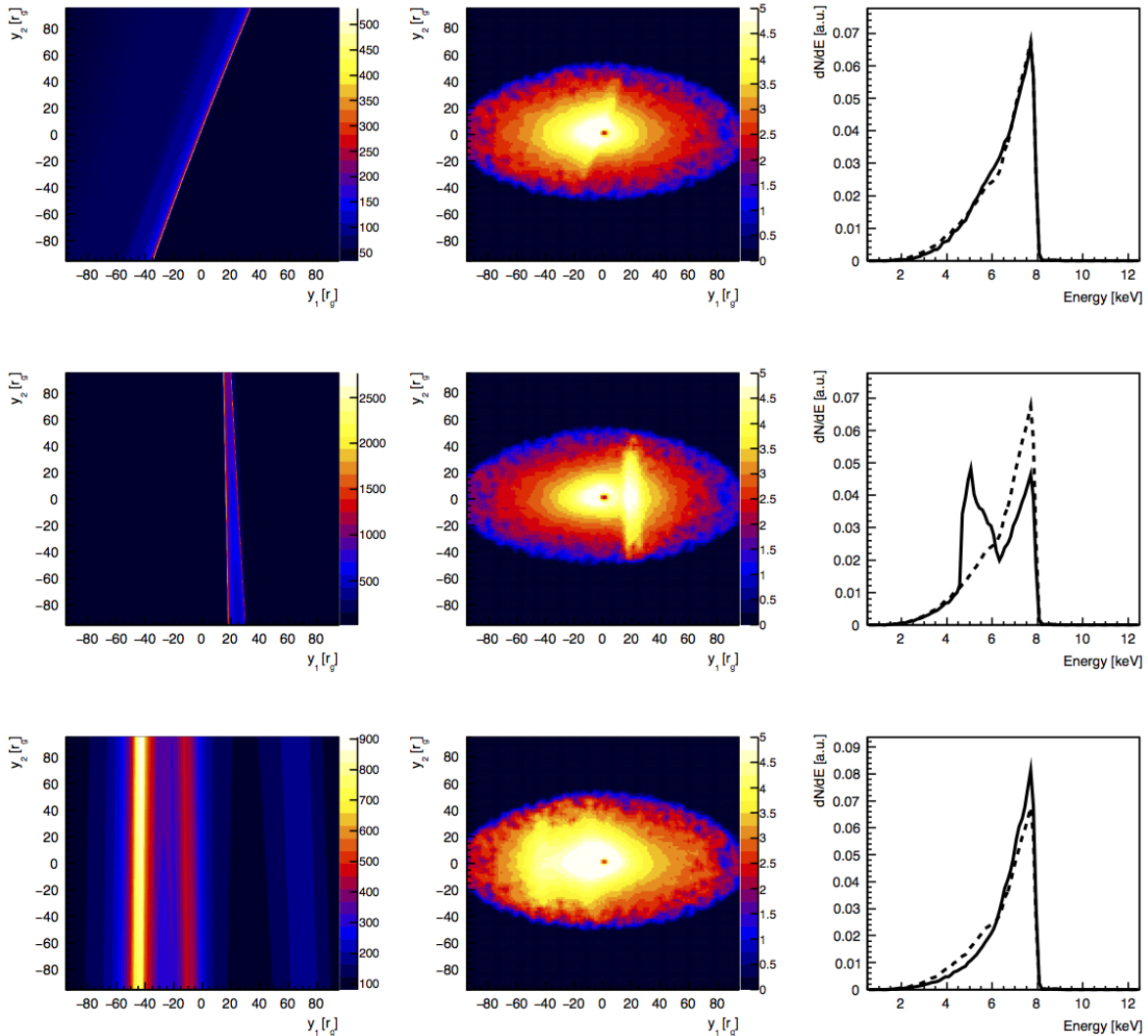


Figure 7. The left panels show small regions of the magnification map for image A of RX J1131–1231, with $g_* = 5\%$ ($\kappa_c = 0.42$, $\gamma = 0.597$, and $\kappa_* = 0.0221$). The center panels show the virtual images of the Fe $K\alpha$ surface brightness convolved with the magnification pattern from the left panels. The right panels show the resulting Fe $K\alpha$ energy spectra before (dashed lines) and after (solid lines) accounting for the microlensing magnification. We normalize all energy spectra to the same total flux to facilitate the comparison of their shapes. All figures are shown for spin parameter of $a = 0.9$, a lamppost corona at $h = 5r_g$, and an inclination angle of $i = 62.5^\circ$.

magnification maps on the relevant spatial scales of a few $10 r_g$'s, and explore how they distort the energy spectra of the microlensed Fe $K\alpha$ emission for a black hole with $r_g = 0.00096$ in dimensionless units, spin $a = 0.9$ in geometrical units, a lamppost corona at $h = 5r_g$. Furthermore, we assume that the shear direction is aligned with the spin axis of the black hole, as caustics perpendicular to the accretion disk tend to maximize the spectral distortions.

Figure 7 shows random locations of the magnification maps (left panels), the Fe $K\alpha$ emissivity convolved with these magnification maps (center panels), and the result-

ing Fe $K\alpha$ energy spectra (right panels) for Image A with $g_* = 5\%$. The upper panel of Figure 7 shows a map with a rather simple caustic structure selectively amplifying the emission from certain portions of the accretion disk leading to a somewhat distorted energy spectrum. The center panel of Figure 7 shows that the microlensing can produce energy spectra with multiple pronounced peaks. The lower panel of Figure 7 shows that many caustics do not necessarily lead to more extreme spectral distortions, as the superposition of the caustics leads to a more uniform magnification of the disk emission than a single caustic.

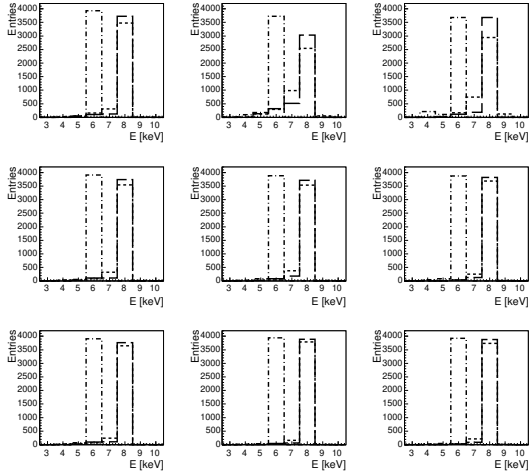


Figure 8. Distribution of the line centroid energies for the simulations of image A of RX J1131–1231 for the microlensing models shown in Figure 3 and a black hole inclination of 2.5° (dot-dashed line), 62.5° (long-dashed line) and 82.5° (short-dashed line) for different splits of the total convergence κ between stellar convergence $\kappa_* = g_*\kappa$ and smooth convergence $\kappa_c = (1 - g_*)\kappa$ with $g_* = 0.025, 0.05, 0.1, 0.25, 0.5, 0.75, 0.9, 0.95,$ and 0.975 (starting in the upper left corner and going row-wise from the left to the right). As in the previous figures, a spin parameter of $a = 0.9$ is chosen and the lamppost corona is located at $h = 5r_g$. The energies are give in the quasar reference frame.

We perform a qualitative analysis of the simulated Fe K α energy spectra with a simple algorithm finding the highest peak of each simulated energy spectrum, and searching for a secondary peak with a peak flux value exceeding by 4% of the primary peak flux amplitude in the valley between the primary and secondary peaks. Figure 8 shows the distribution of the peaks of the Fe K α energy spectra as function of g_* (image A of RX J1131–1231 and black hole inclinations of $2.5^\circ, 62.5^\circ$ and 82.5°). The three energy spectra with $g_* \leq 10\%$ are most strongly affected by the microlensing. The models for $g_* = 5\%$ and $g_* = 10\%$ show that the microlensing has some -albeit limited- impact on the line centroid distribution.

Figure 9 presents the distribution of the peaks of the Fe K α emission for several black hole spins. The distribution is always strongly peaked around the peak energy of the unlensed emission, which shifts slightly from lower to higher energies as the black hole spin increases. Figure 10 shows how the distribution changes when the mass of the black hole (giving physical size of the accretion system) is changed by a factor λ , or, alternatively the mass scale of the deflecting stars is changed by a factor $\lambda^{1/2}$. Although λ does impact the distribution somewhat, the main characteristic (i.e. a pronounced

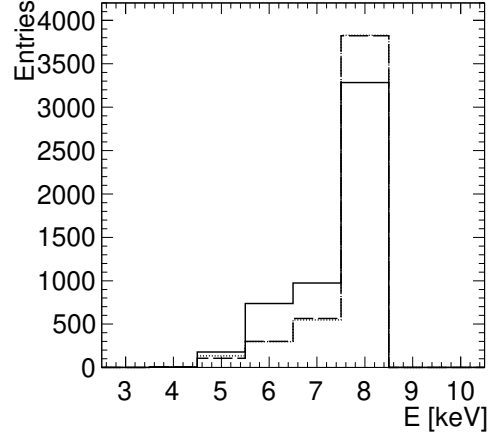


Figure 9. Distribution of the line centroid energies for the simulations of image A of RX J1131–1231 with $g_* = 5\%$ for a black hole spin a of 0 (solid line), 0.9 (long-dashed line), and 0.998 (dotted line). All distributions assume a lamppost corona at $h = 5r_g$ and an inclination angle of $i = 62.5^\circ$. The energies are give in the quasar reference frame.

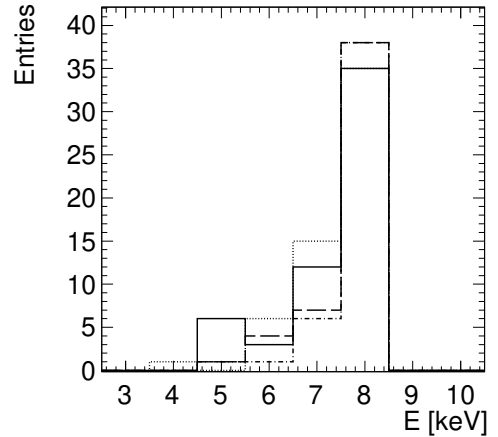


Figure 10. Distribution of the line centroid energies for the simulations of image A of RX J1131–1231 with $g_* = 5\%$ scaling the mass of the black hole by λ , or, alternatively with mass scale of the deflecting stars by $\lambda^{-1/2}$ with $\lambda = 4$ (solid line), 2 (dotted), 1 (long-dashed), and 0.67 (dashed-dotted). All distributions assume a black hole spin parameter of $a = 0.9$, a lamppost corona at $h = 5r_g$, and an inclination angle of $i = 62.5^\circ$. The energies are give in the quasar reference frame.

peak at the energy of the peak of the distribution without gravitational lensing) remains unaffected.

As expected from Figure 4, the minimum image B (and similarly image C) is much less affected by microlensing as the source plane density of caustics is much smaller, and it is correspondingly less likely that the central portion of the accretion disk intercepts a caustic fold or cusp. The peak energies (not shown here) are narrowly distributed around the value without gravitational lensing.

6. COMPARISON BETWEEN SIMULATIONS AND CHANDRA OBSERVATIONS

The simulated line centroid distributions of Figures 8-10 cannot be directly compared to the observed distribution of Fig. 2, as the latter are affected by detection biases resulting for example from *Chandra's* effective area and energy resolution, the energy dependent signal to noise ratio and the particular analysis choices. We performed a first analysis that accounts for these biases by converting the simulated Fe $K\alpha$ energy spectra into simulated *Chandra* data sets, and by applying an automatized search for emission lines to these data sets.

The HEASARC (High Energy Astrophysics Science Archive Research Center) software (i.e. the *table* class of the HEASPC package) is used to generate a table model for each simulated Fe $K\alpha$ energy spectrum. A model consisting of an absorbed powerlaw model plus the Fe $K\alpha$ energy spectrum is subsequently defined in the *Xspec* fitting package Arnaud et al. (2017). The *Xspec* command *fake* is subsequently used to generate a *Chandra* energy spectrum. Hereby the overall normalization of the Fe $K\alpha$ line flux is treated as an adjustable parameter.

The automatic search for Fe $K\alpha$ lines is performed with a Tool Command Language (*TCL*) script. The script first fits an absorbed powerlaw model. Subsequently, it iterates over the starting value E_1 of the centroid energy of an added Gaussian emission line from 1.5 keV to 6 keV in 0.1 keV steps (observer frame energies). The script identifies the best fit and estimates the statistical evidence for a line detection from Fisher statistic. The iteration over E_1 is followed by the iteration over the line centroid energy E_2 of a second line. The algorithm again identifies the best fit and evaluates Fisher statistic to obtain a measure for the statistical significance of the detection of a second line.

It is well known that the Fisher statistic under or overestimate the chance probability of certain spectral features Protassov et al. (2002). This does not matter here, as we are only interested in the comparison of the results obtained for the observed and simulated data. We choose a threshold value of the Fisher statistic, so that the automatic script gives approximately the same num-

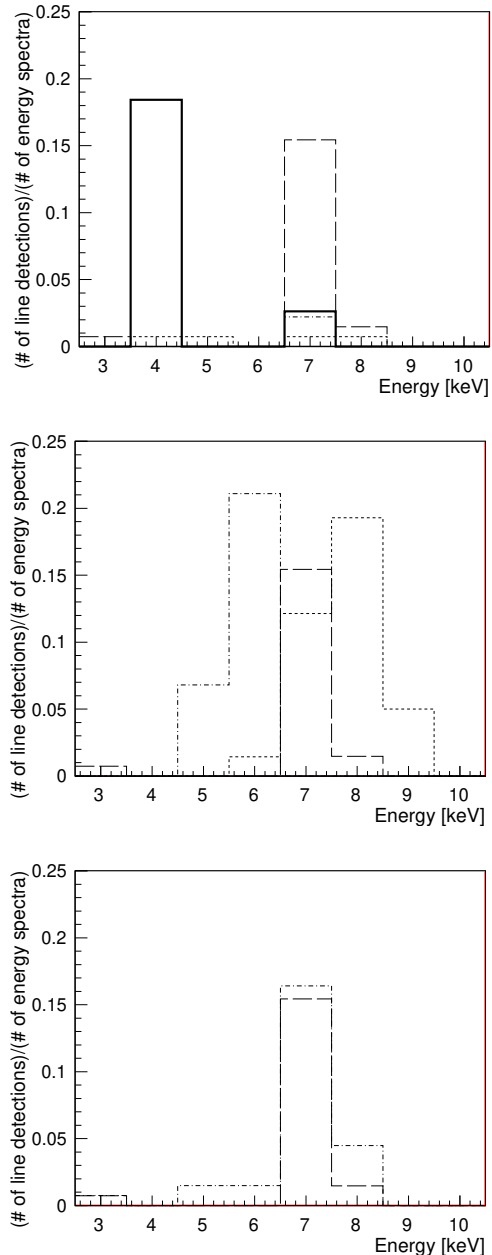


Figure 11. The upper panel shows the line energies found by the automated analysis script in the observed RX J1131–1231 data set (thick solid line) and in the simulated data sets (thin lines) for image A of the source (all energies are in the quasar reference frame). The simulations are for a black hole spin of $a = 0.9$, inclination of $i = 62.5^\circ$, and microlensing with $g_* = 5\%$. The thin lines show the results for different choices of the line intensities varying by a factor of two between adjacent lines. The center panel presents simulated results for black hole inclinations of 2.5° (dashed-dotted line), 62.5° (long-dashed line), and 82.5° (short-dashed line). The lower panel shows simulated results for $i = 62.5^\circ$ for two different microlensing parameters: $g_* = 0.025$ (dashed-dotted line) and 0.05 (long-dashed line).

ber of lines when applied to the observed *Chandra* data as the manual analysis.

The automated analysis is identically applied to the observed and simulated data sets. The thick solid line in the upper panel of Figure 11 shows the distribution of the lines detected by the automated script in the observed spectra of RX J1131–1231. The results can be compared to those from the manual analysis in Fig. 2. Although both analyses find most line centroids at source frame energies around ~ 4 keV, the automated script finds a significantly larger fraction of lines at 4 keV than at 7 keV in image A of RX J1131–1231 compared to the manual spectral analysis. Part of the difference results from the fact that the confidence levels are derived more rigorously in the manual approach which makes use of Monte Carlo simulations than the automated approach which use the less reliable Fisher statistic.

From bottom to top, the dotted (barely visible), short-dashed, dashed-dotted, and long-dashed lines show the spectral lines found in the simulations for image A for different Fe $K\alpha$ emission strengths increasing from line to line by a factor of 2. The data and simulation histograms are normalized to the number of analyzed energy spectra, so that the shapes and absolute values of the distributions can be compared to each other. If we adjust the flux normalization of the Fe $K\alpha$ emission so that we get approximately the same number of detections as in the observed RX J1131–1231 data set, the simulations predict line detections narrowly clustered around line energies of 7 keV. The distribution deviates significantly from the distribution of lines detected by the manual and automated analyses in the real *Chandra* data. In particular, the simulations do not reproduce the frequent detection of lines around 4 keV.

The center panel of Fig. 11 shows the fitted line centroids for different simulated inclinations. For each inclination we chose a representative Fe $K\alpha$ intensity which gives roughly the right number of line detections. At the lower inclinations, the line centroids shift towards lower energies, but still do not reproduce the large number of lines detected around 4 keV.

The lower panel of Fig. 11 shows that the simulations for different g_* -values give very similar line centroid distributions – once we adjust the Fe $K\alpha$ intensity appropriately. The microlensing has a rather limited impact on the detected line centroid distribution.

We present the comparison between the simulated and observed line centroid distributions for images B, C, and D in Figure 12. For images B and D the simulated distributions clearly underpredict the number of line detections at < 5 keV energies.

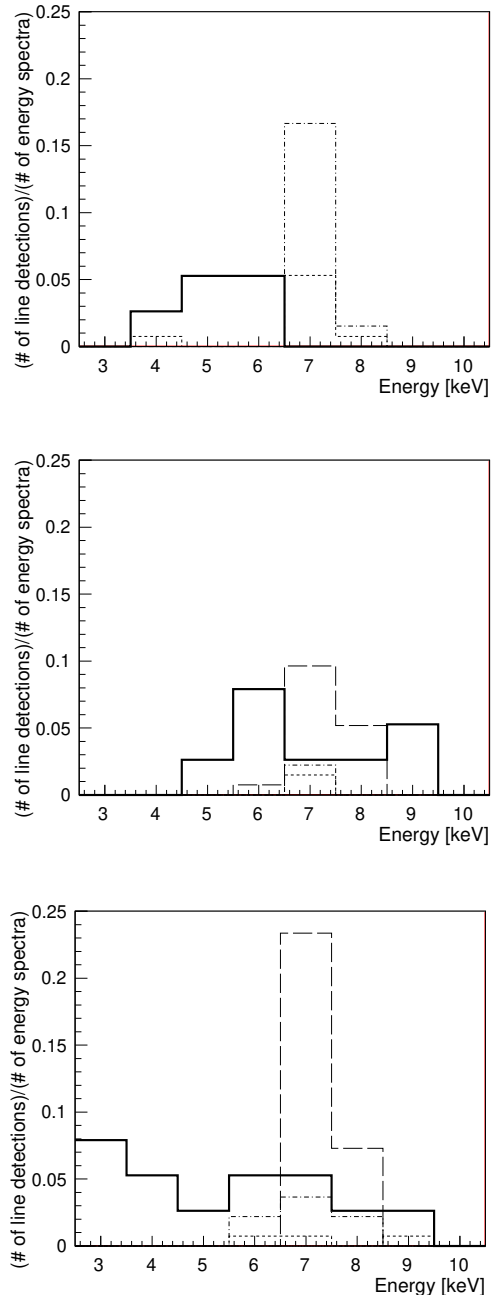


Figure 12. Same as the top panel of Fig. 11 but for images B (top), C (center) and D (bottom).

We checked the results for different black hole spins and got similar results. For lower (higher) spin parameters, the centroid distributions are slightly narrower (wider) than for the spin parameter $a = 0.9$ - but without substantially affecting the mismatch between the simulations and the observations.

7. SUMMARY AND DISCUSSION

It is instructive to point out similarities and differences between this paper discussing the distribution of the spectral shapes of the Fe $K\alpha$ emission from microlensed quasars and earlier papers discussing the statistical distribution of brightness fluctuations caused by microlensing (e.g. Schechter & Wambsganss 2002; Pooley et al. 2012) and the detailed modeling of the microlensed light curves (e.g. Lewis & Irwin 1996; Dai et al. 2010). The distribution of the magnification factors does not depend on the spatial (or angular) scale of the magnification maps relative to the spatial scale of the quasar accretion disk, as long as the Einstein radius of the deflectors is much larger than the sizes of the emitting regions. The unitless lens equation used to model the distribution of magnification factors does indeed not depend on the mass scale of the deflectors $\langle m_* \rangle$. In contrast, the modeling of the microlensed light curves does depend on the spatial scale of the magnification maps, as the time between caustic crossings depends on this scale divided by the velocity of the deflectors perpendicular to the line of sight. In the case considered here, the results depend on the spatial scale of the magnification maps as well, as the spatial scale impacts the expected number of caustics intersecting the central portion of the accretion flow.

The simulations show that microlensing can modify the energy spectra of the observed Fe $K\alpha$ emission, but the effect is not large enough to explain the range of the observed line energies (Figures 11 and 12). In particular, the simulations do not reproduce the highly redshifted peaks with <5 keV centroids seen in the data. The overall small impact of the microlensing on the observed distribution of line energies has several explanations. For microlensing maps with a low density of caustics, the caustics do not intersect the inner accretion flow often enough. For microlensing maps with a high densities of caustics, we observe rather small distortions of the Fe $K\alpha$ lines when compared to the statistical uncertainties in the *Chandra* data. Another contributing effect is that microlensing most likely leads to a line detection when

the brightest emission is amplified, giving a line detection with a centroid similar to that of the unlensed Fe $K\alpha$ emission.

Our simulations have several shortcomings. We have not modeled the spatial extent of the corona, and we did not model the microlensing of the direct corona emission. Furthermore, we describe the emitted Fe $K\alpha$ energy spectrum in the rest frame of the accreting plasma with a delta-function in energy (see García et al. (2016), and references therein for more realistic emission energy spectra). We choose for each observation a random patch from a large magnification map, assuming that the caustics move relatively fast relative to the quasar so that each *Chandra* observation catches a different region of the caustic net. In reality, the caustics may move relatively slowly so that multiple *Chandra* observations are affected by a single caustic structure. The geometry of the accretion disk may differ from the paper-thin geometry assumed here. The disk may be geometrically thick, it may be patchy, or partially obscured. The geometry of the inner accretion flow of powerful sources like RX J1131–1231 may differ from that of the well studied nearby Seyfert 1 galaxies. If the black hole is sufficiently more massive than what we assume, it would intersect a larger number of caustics. Last but not least, our microlensing model may be insufficient. For example, Dai & Guerras (2018) propose that planets in the lensing galaxy may produce caustics with observable signatures. We plan to evaluate the impact of these effects in our future work.

ACKNOWLEDGMENTS

HK would like to thank NASA (grant #NNX14AD19G) and the Washington University McDonnell Center for the Space Sciences for financial support. GC would like to acknowledge financial support from NASA via the Smithsonian Institution grants SAO GO4-15112X, GO3-14110A/B/C, GO2-13132C, GO1-12139C, and GO0-11121C. HK thanks Quin Abarr for implementing the Cash-Karp integration of the geodesics into the ray tracing code.

REFERENCES

- Arnaud, K., et al. 2017, <https://heasarc.gsfc.nasa.gov/xanadu/xspec/>
- Beheshtipour, B., Hoormann, J., Krawczynski, H. 2016, *ApJ*, 826, 203
- Beheshtipour, B., Krawczynski, H., Malzac, J. 2017, *ApJ*, 850, 14
- Blackburne, J. A., Kochanek, C. S., Chen, B., Dai, X., Chartas, G. 2015, *ApJ*, 798, 95
- Blackburne, J. A., Pooley, D., Rappaport, S., Schechter, P. L. 2011, *ApJ*, 729, 34
- Blandford, R., Narayan, R. 1986, *ApJ*, 310, 568
- Cackett, E. M., Zoghbi, A., Reynolds, C., Fabian, A. C., Kara, E., Uttley, P., Wilkins, D. R. 2014, *MNRAS*, 438, 2980
- Chandrasekhar, S. 1960, *Radiative Transport*, (New York: Dover)

- Chartas, G., Agol, E., Eracleous, M., et al. 2002, *ApJ*, 568, 509
- Chartas, G., Kochanek, C. S., Dai, X., Poindexter, S., Garmire, G. 2009, *ApJ*, 693, 174
- Chartas, G., Kochanek, C. S., Dai, X., Moore, D., Mosquera, A. M., Blackburne, J. A. 2012, *ApJ*, 757, 137
- Chartas, G., Krawczynski, H., Zalesky, L., et al., “Measuring the Innermost Stable Circular Orbits of Supermassive Black Holes”, *ApJ* **837**, 26 (2017) (C17).
- Chiang, C.-Y., Walton, D. J., Fabian, A. C., Wilkins, D. R., & Gallo, L. C. 2015, */mnras*, 446, 759
- Dai, X., Kochanek, C. S., Chartas, G., et al. 2010, *ApJ*, 709, 278
- Dai, X. & Guerras, E. 2018, *ApJL*, 853, L27
- Fabian, A. C., Fabian, A. C., Iwasawa, K., Reynolds, C. S., Young, A. J. 2000, *PASP*, 112, 1145
- Fabian, A. C., Zoghbi, A., Ross, R. R., et al. 2009, *Nature*, 459, 540
- Faure, C., Anguita, T., Eigenbrod, A., Kneib, J.-P., Chantry, V., Alloin, D., Morgan, N., Covone, G. 2009, *A&A*, 496, 361
- Fohlmeister, J., Kochanek, C. S., Falco, E. E., Morgan, C. W., Wambsganss, J. 2008, *ApJ*, 676, 761
- Fohlmeister, J., Kochanek, C. S., Falco, E. E., Wambsganss, J., Oguri, M., Dai, X. 2013, *ApJ*, 764, 186
- García, J. A., Fabian, A. C., Kallman, T. R., Dauser, T., Parker, M. L., McClintock, J. E., Steiner, J. F., Wilms, J. 2016, *MNRAS*, 462, 751-760.
- Gould, A. 2000, *ApJ*, 535, 928
- Hogg, D. W. 2000, “Distance measures in cosmology”, [arXiv:astro-ph/9905116v4](https://arxiv.org/abs/astro-ph/9905116v4)
- Hoormann, J. K., Beheshtipour, B., & Krawczynski, H. 2016, *PhRvD*93, 044020
- Jiménez-Vicente, J., Mediavilla, E., Kochanek, C. S., Muñoz, J. A. 2016, *ApJ*, 799, 149
- Jovanović, P., Popović, L. Č, Simić, S. 2009, *New Astron. Rev.*, 53, 156
- Kayser, R., Refsdal, S., Stabell R. 1986, *A&A*, 166, 36
- Keeton, C. R. 2001, *Computational Methods for Gravitational Lensing*, [arXiv:astro-ph/0102340](https://arxiv.org/abs/astro-ph/0102340)
- Kochanek, C. S., Dalal, N. 2004, *ApJ*, 610, 69
- Krawczynski, H. 2012, *ApJ*, 754, 133
- Krawczynski, H. 2018, *Gen. Rel. & Grav.*, Vol. 50, Iss. 8, article id. 100
- Krawczynski, H., Chartas, G. 2017, submitted to *ApJ*, <http://lanl.arxiv.org/abs/1610.06190>
- Lewis, G. F., Irwin, M. J. 1996, *MNRAS*, 283, 225
- Matt, G., Perola, G. C., & Piro, L. 1991, *A&A*, 247, 25
- MacLeod, C. L., Morgan, C. W., Mosquera, A., et al. 2015, *ApJ*, 806, 258
- Metcalf, R. B., Madau, P. 2001, *ApJ*, 563, 9
- Morgan, C. W., Kochanek, C. S., Morgan, N. D., & Falco, E. E. 2010, *ApJ*, 712, 1129
- Morgan, C. W., Hainline, L. J., Chen, B., et al. 2012, *ApJ*, 756, 52
- Mosquera, A. M., Kochanek, C. S., Chen, B., Dai, X., Blackburne, J. A., Chartas, G. 2013, *ApJ*, 769, 53
- Neronov, A., Vovk, I., *PhRvD* **93**, 023006 (2016).
- Paczynski, B. 1986, *ApJ*, 301, 503
- Parker, M. L., Wilkins, D. R., Fabian, A. C., et al. 2014, *MNRAS*, 443, 1723
- Peebles P. J. E. 1993, “Principles of Physical Cosmology”, Princeton University Press, Princeton
- Planck Collaboration, Ade, P. A. R., Aghanim, N., Arnaud, M. 2016, *A&A*, 594, 13
- Poindexter, S., Kochanek, C. S. 2010, *ApJ*, 712, 658
- Pooley, D., Rappaport, S., Blackburne, J. A., Schechter, P. L., Wambsganss, J. 2012, *ApJ*, 744, 111
- Popović, L. Č, Mediavilla, E., Jovanović, Muñoz, J. A. 2003, *A&A* 398, 975
- Popović, L. Č, Jovanović, Mediavilla, E., Zakharov, A. F., Abajas, C., Muñoz, J. A., Chartas, G. 2006, *ApJ*, 637, 620
- Protassov, R., van Dyk, D. A., Connors, A., Kashyap, V. L., Siemiginowska, A. 2002, *ApJ*, 571, 545
- Reynolds, C. S. 2014, *SSRv*, 183, 277
- Schechter, P. L., Wambsganss, J. 2002, *ApJ*, 580, 685
- Schechter, P. L., Wambsganss, J., Lewis, G. F. 2004, *ApJ*, 613, 77
- Schechter, P. L., Wambsganss, J. 2004, in *IAU Symp. 220, Dark Matter in Galaxies*, ed. S. D. Ryder et al. (San Francisco, CA: ASP), 103
- Schechter, P. L., Pooley, D., Blackburne, J. A., Wambsganss, J. 2014, *ApJ*, 793, 96
- Schneider, P., Ehlers, J., & Falco, E. E. 1992, *Gravitational Lenses*, XIV, 560, pp. 112 figs.. Springer-Verlag Berlin Heidelberg New York. Also *Astronomy and Astrophysics Library*
- Schneider, P., Weiss, A. 1987, *A&A*, 171, 49
- Tewes, M., Courbin, F., Meylan, G. 2013, *A&A*, 556, 22
- Uttley, P., Cackett, E. M., Fabian, A. C., Kara, E., Wilkins, D. R. 2014, *A&ARv*, 22, 72
- Wambsganss, J. 1999, *J. of Comp. and Appl. Math.*, 109, 353

- Wambsganss, J. 2006, In: Gravitational lensing: strong, weak and micro. Saas-Fee Advanced Course 33. The Course took place from 8-12 April 2003, in Les Diablerets, Switzerland. Swiss Society for Astrophysics and Astronomy. Edited by G. Meylan, P. Jetzer and P. North. Lecturers: P. Schneider, C. Kochanek, J. Wambsganss. Berlin: Springer, ISBN 3-540-30309-X, ISBN 978-3-540-30309-1, p. 453
- Wambsganss, J., Paczynski, B. 1992, ApJ, 397, L1
- Webster, R. L., Ferguson, A. M. N., Corrigan, R. T., Irwin, M. J. 1991, AJ, 102, 1939
- Wilms, J., Reynolds, C. S., Begelman, M. C., et al. 2001, MNRAS, 328, L27
- Witt, H. J. 1993, ApJ, 403, 530
- Yonehara, A., Umemura, M., Susa, H. 2003, PASJ, 55, 1059
- Young, P. 1981, ApJ, 244, 756
- Zoghbi, A., Fabian, A. C., Uttley, P., et al. 2010, MNRAS, 401, 2419
- Zoghbi A., Fabian A. C., Reynolds C. S., Cackett E. M. 2014, MNRAS, 422, 129